Reverse-time ray-tracing method for microseismic source localization

Liang Ding,[1] Er-gen Gao,[2] Qinya Liu,[3] Wei Qian,[1] Dongdong Liu[4] and Chi Yang[5]

[1]*School of Earth Sciences and Engineering, Hohai University, Nanjing 211000, China*
[2]*Anhui Jianzhu University, Hefei 230601, China. E-mail: gaoergen@126.com*
[3]*Department of Physics & Department of Earth Sciences, University of Toronto, Toronto M5S 1A7, Canada*
[4]*Changshu Seismic Station, Jiangsu Earthquake Administration, Changshu 215500, China*
[5]*Earthquake Administration of Jiangsu Province, Nanjing 210014, China*

SUMMARY

Accurate source localization is a critical component of seismic monitoring. The efficiency of location algorithms is limited by several factors, such as the dimension of source parameter search space and iterative procedures of the algorithm. To avoid iterations and accelerate source localization algorithms, a reverse-time ray tracing method (RTRTM) is presented. The RTRTM estimates the particle motion direction and arrival time based on the polarization scanning method, and calculates the incident *P*-wave polarization vector based on the near-surface structure. It then back-traces trajectories of *P* waves based on the reversed direction of incident *P*-wave polarization vectors, and locates the mean position of converging ray terminals as the source position and the corresponding time as the original time of the event. The accuracy and efficiency of the RTRTM method are demonstrated by the source localization results of both synthetic data and data from an $M_b = 1.6$ local earthquake. The reliability of polarization estimation method and the effect of velocity structures on RTRTM source localization are also discussed.

Key words: Body waves; Computational seismology; Induced seismicity; Theoretical seismology; Time-series analysis; Seismic noise.

1 INTRODUCTION

Accurate source localization is essential in microseismic monitoring as it provides valuable information about the seismicity induced by anthropogenic activities, such as in hydraulic fracturing monitoring (Duncan & Eisner 2010; Maxwell *et al.* 2010; Ellsworth 2013) and CO_2 storage monitoring (Oye & Roth 2003; Goertz-Allmann *et al.* 2014; Jones *et al.* 2014). Similarly, accurate source parameters also help reveal the location and distribution of natural phenomena, such as glacial earthquakes (Larmat *et al.* 2008).

Source locations are generally determined by two main types of source localization algorithms, either waveform-based methods or ray-based methods. Relying on the seismic wave equation, the waveform-based methods try to focus the energy of seismic waves back to the hypocentre by reverse-time extrapolation of waveforms from receivers (Artman *et al.* 2010; Haldorsen *et al.* 2013; Grigoli *et al.* 2014). Because they do not require arrival time picking and polarization estimation of seismic phases, the waveform-based methods have shown robustness and reliability in long-period event localization (O'Brien *et al.* 2011) and microseismic source imaging (Folesky *et al.* 2015; Price *et al.* 2015). However, the waveform-based methods face several limitations. For example, they typically require highly accurate background velocity models, and the full numerical simulation of seismic waves can be time-consuming especially in 3D cases even with parallel computing (Shi & Wang 2012) and GPU capabilities (Xue *et al.* 2016) employed to accelerate the simulations.

In comparison, the alternative ray-based methods only need to identify and pick seismic phases, and then seek to minimize traveltime differences between the observed and calculated seismic phases by adjusting the source position and origin time. However, microseismic records often have relatively low signal-to-noise ratio, which makes it difficult to identify and pick seismic phases directly from the records. Therefore, improved methods based on the Akaike information criteria have been proposed as phase picker to identify seismic phases (Akaike, 1998; Zhang *et al.* 2003; Grigoli *et al.* 2014; Hirabayashi 2016; Li *et al.* 2017).

More recently, multiple-component sensors are widely used for microseismic monitoring. Three-component (3-C) records can be used to facilitate the picking of phases and estimate polarization directions of arrivals. For example, Saari (1991) used maximum likelihood technique to estimate the polarization azimuth of *P* waves by a single 3-C station. Moriya *et al.* (1994) applied the spectral matrix to estimate the direction of particle motion in the time–frequency domain for accurate source localization. Vidale (1986) and Jurkevics (1988) project the 3-C recordings on to three orthogonal directions to build the covariance matrix and calculate the eigenvalues and eigenvectors. The eigenvectors
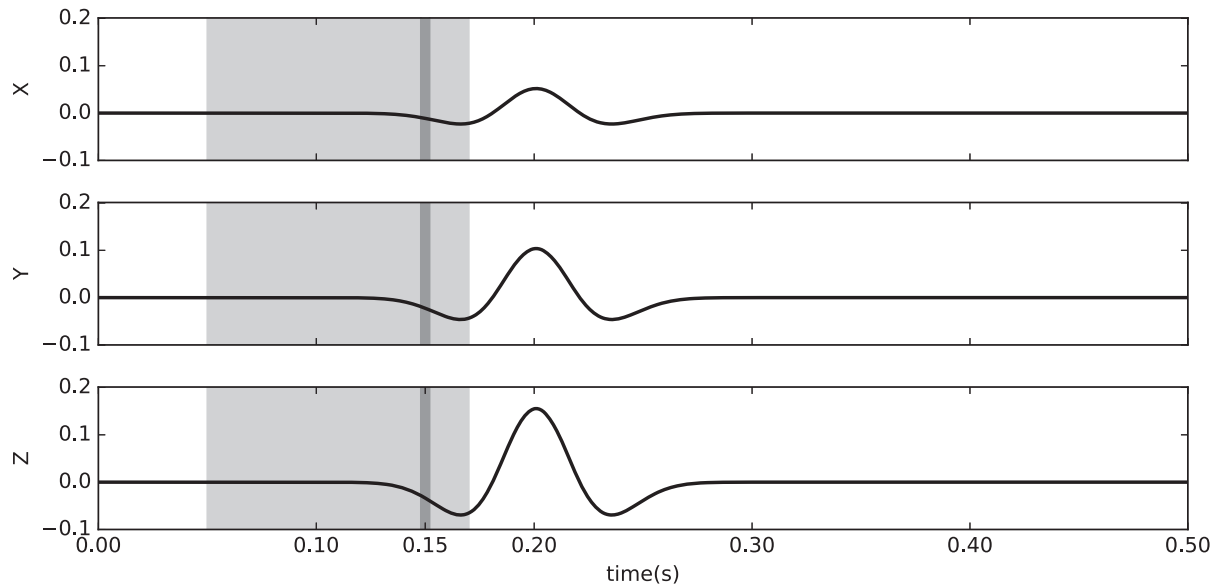
Figure 1. Three-component synthetic waveforms based on a Ricker wavelet of 20-ms half duration. The light-grey time window represents the scanning range while the dark-grey slim window represents the sliding window with a length of 4 ms.
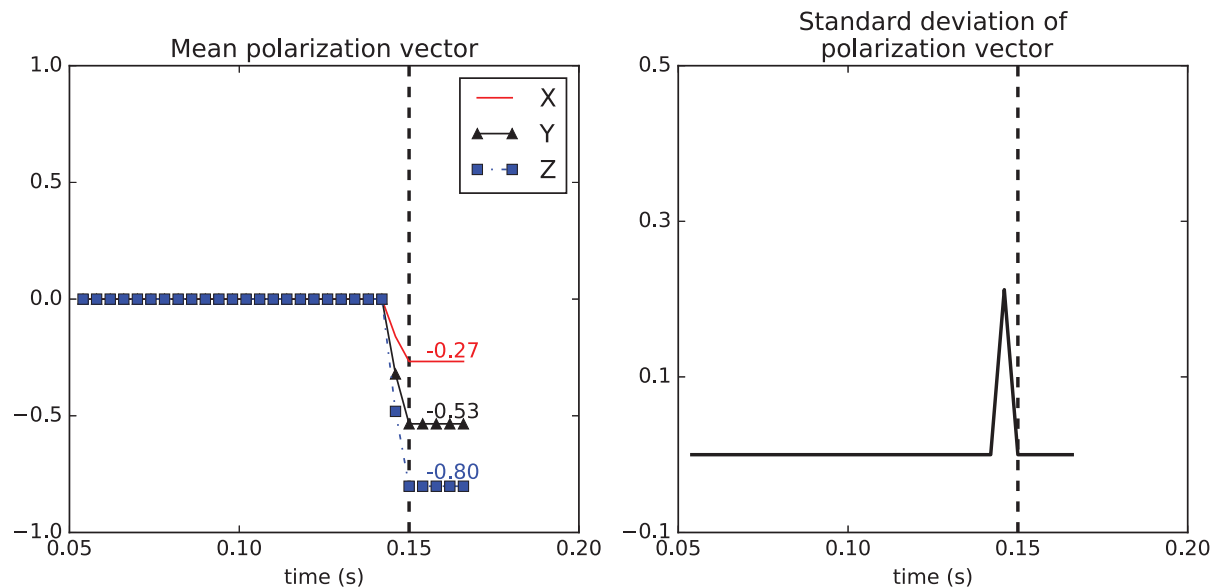
Figure 2. Three-component mean (left) and standard deviation (right) of the polarization vectors as a function of central time of sliding windows in Fig. 1. The dashed line marks the time when the standard deviation of polarization vector first reaches to minimum after the phase starts to arrive. The polarization vector of this phase is selected to be $(-0.27, -0.53, -0.80)$ at $0.15\ s$.

associated with the largest eigenvalue is the direction of the largest amount of polarization. Bayer *et al.* (2012) used this method to estimate the azimuth of *P* wave to track unilateral earthquake rupture. Oye & Roth (2003) determined the *P* polarization from the solution of the co-variance matrix of the microseismic three-component ground motion data for a time window enclosing the *P*-wave signal. Galiana-Merino *et al.* (2007) used an adaptive-length window to scan 3-C seismograms in the time range containing the first-break to estimate the polarization azimuth after reducing the noise using wavelet packet transforms (Galiana-Merino *et al.* 2003). Bayer *et al.* (2012) use 3-C recording samples in a 60 s length sliding window to construct a covariance matrix and to calculate the polarization parameters, and study the changes of polarization caused by the propagating rupture of earthquake. The principal component analysis (PCA) introduced by Pearson (1901) can be used to estimate the principle direction of seismic wave using 3-C data by projecting the 3-C surface recordings on to the horizontal plane and vertical direction. For example, Park & Ishii (2018) projected the surface 3-C seismograms on to the vertical-radial plane to construct the covariance matrix and define the first principal component of the observed particle motions as the apparent polarization direction for 3C teleseismic body-wave arrivals.

   With traveltime of seismic phases are determined, the ray path and traveltime difference between the *S*- and *P*-phase can be used to locate microseismic sources based on the assumption of a homogeneous background velocity model (Oye & Roth 2003). More sophisticated
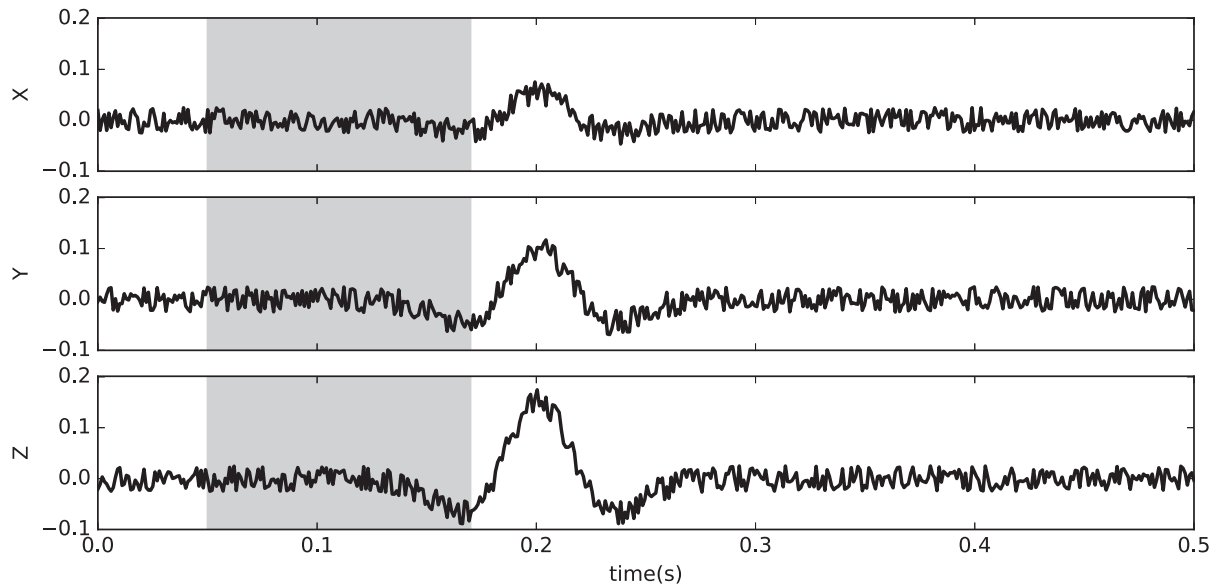
Figure 3. Three-component noisy waveforms generated by adding Gaussian random noise to the original waveforms in Fig. 1.
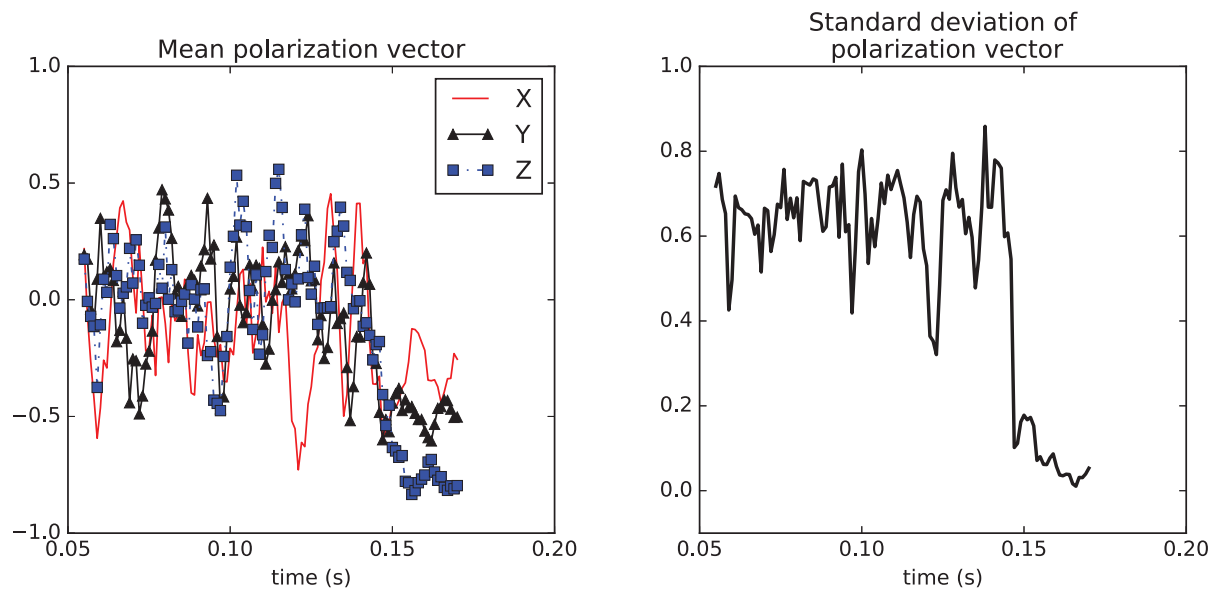

Figure 4. Three-component mean (left) and standard deviation (right) of polarization vectors as a function of time.

structural models have been proposed for microseismic source localization, such as 1-D velocity models (Jansky *et al.* 2010; Jones *et al.* 2014), 1-D anisotropy models (King & Talebi 2007), blocking models (Xu *et al.* 2006) and 3-D velocity models (Gambino *et al.* 2004). For complex background velocity models, seismic ray-tracing methods, such as two-point ray-tracing method (Buland & Chapman 1983; Um & Thurber 1987; Bulant 1996; Cerveny *et al.* 2005; Gao *et al.* 2002, 2007, 2008), finite-difference methods (Miksat *et al.* 2008), graph-theory ray-tracing methods (Bai *et al.* 2010) and fast-marching algorithms (Sethian & Popovici 1999) may need to be used to obtain ray trajectories and traveltimes of seismic phases. Source locating process can be performed for single station using the phase azimuth and time difference between *P* and *S* waves (Magotra *et al.* 1989; Saari 1991). The inaccuracy of traveltime and polarization deteriorates the locating results. The locating process based on the arrival time or polarization for multiple station requires iteration. For example, Oye & Roth (2003) use grid search and the neighbourhood algorithm to locate the microseismic source position using the polarity of *P*-waves and the traveltimes of *P* and *S* waves. Grigoli *et al.* (2014) use grid search to calculate the stack of STA/LTA traces according to theoretical arrival time for both *P* and *S* phases, and find the position with maximum stacking amplitude as the source location. Tan *et al.* (2017) use the polarization and traveltime of *P* and *S* waves to build the cost function and use improved grid search to find the microseismic source position. These type of location methods requires large amount of computational time to find the position at which the synthetic traveltimes or polarizations of seismic phases fit best to those of the observing data.
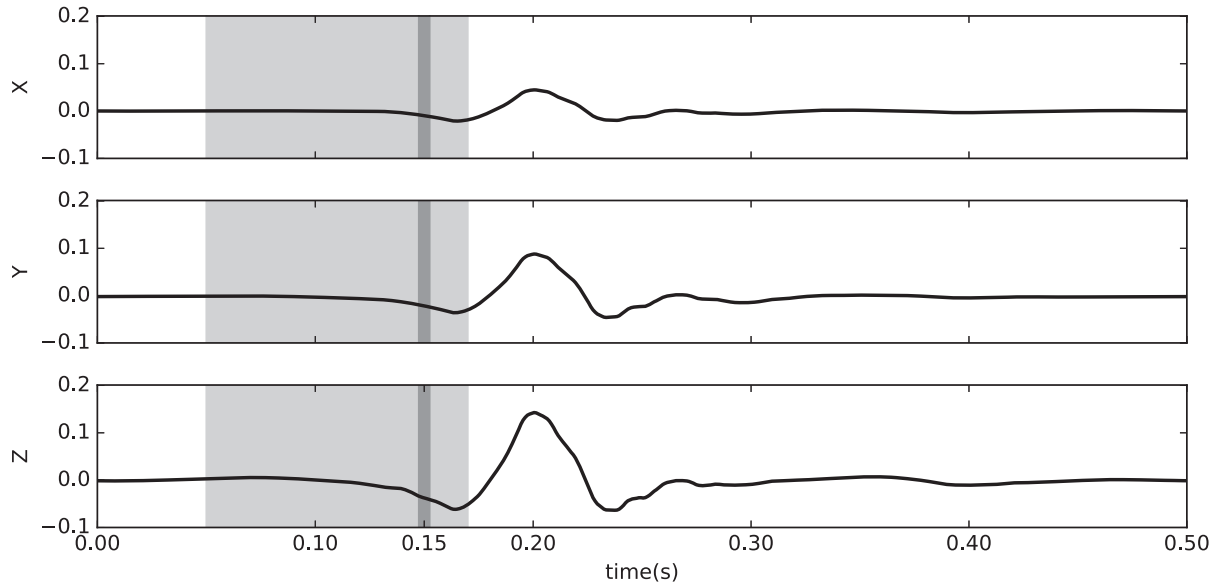
Figure 5. Three-component denoised waveforms based on DWT. The light-grey box represents the scanning time range. The dark-grey slim box represents a scanning window length with a length of 4 ms. The centre of this particular scanning window gives the arrival time of the phase (see also Fig. 6).

To increase the efficiency of source localization, we propose a reverse-time ray-tracing method (RTRTM). It estimates the particle motion direction based on polarization scanning method and calculates the incident *P* ray vector based on near-surface structures. It then back-traces the trajectories of *P* rays in reverse time for several stations, and uses the time when all ray terminals converge as the source origin time and the mean position of ray terminals as the source position. This paper will first present the polarization scanning method used to estimate arrival polarization, and then give a full description of the RTRTM which is used later for source localization of two synthetic events and a real earthquake.

2 METHODS

2.1 Polarization scanning method

Both traveltime and polarization of the incident *P* waves are affected by the locations of the source and receiver, and the background velocity structures. The particle motion direction caused by the *P* arrivals can be estimated from 3-C recordings. Park & Ishii (2018) pointed out that as the first-arrival particle motion recorded on free surface is the superposition of incident *P* waves, the reflected *P* waves and reflected *SV* waves, the polarization direction of the incident waves is not the same as the surface particle motion direction (also known as apparent polarization direction), and needs to be converted based on near-surface structures (Nagano *et al.* 1989; Shearer 1999). More discussion will be presented in Section 2.3. In the remaining of the section and the synthetic tests in Section 3.1, we ignore the reflected *P* and *S* waves, and do not distinguish between the apparent and true polarization vectors. But in Sections 3.2 and 4, we will apply the proper corrections.

In the following, we examine the time range of 3-C recordings containing the *P* phase to first estimate the particle motion direction at the surface.

For illustration purpose, we first generate a synthetic 3-C time-series using Ricker wavelet as the source-time function (Fig. 1), given by

$$S(t) = (1 - t^2/a^2)e^{-t^2/a^2}, \tag{1}$$

where $a = 20$ ms is the half duration of the central peak. The maximum amplitude ratio of the X, Y, Z component is 1: 2: 3 (Fig. 1) and the time-series sampling interval is 1 ms. We now estimate the polarization of this arrival by first choosing a time range that contains the first half swing of the first-break (indicated by the light-grey box in Fig. 1). Using a sliding window with the length of 4 ms (indicated by the dark-grey range in Fig. 1) and 4 ms moving step, we estimate the polarization for each sample and calculate the mean polarization vector and its standard deviation in the sliding window. The mean polarization vector can be calculated by

$$\overline{\mathbf{V}} = (\overline{r_x}, \overline{r_y}, \overline{r_z}) = \frac{1}{N}\left(\sum_{i=1}^{N}\frac{A_{x_i}}{l_i}, \sum_{i=1}^{N}\frac{A_{y_i}}{l_i}, \sum_{i=1}^{N}\frac{A_{z_i}}{l_i}\right), \tag{2}$$

where $\overline{r_x}, \overline{r_y}, \overline{r_z}$ are the three components of mean polarization vector $\overline{\mathbf{V}}$, N is the number of samples in the sliding window, A_{x_i}, A_{y_i}, and A_{z_i} represent the amplitude of X, Y and Z components of a single sample in seismogram, with norm l_i given by $l_i = (A_{x_i}^2 + A_{y_i}^2 + A_{z_i}^2)^{1/2}$, $i =$
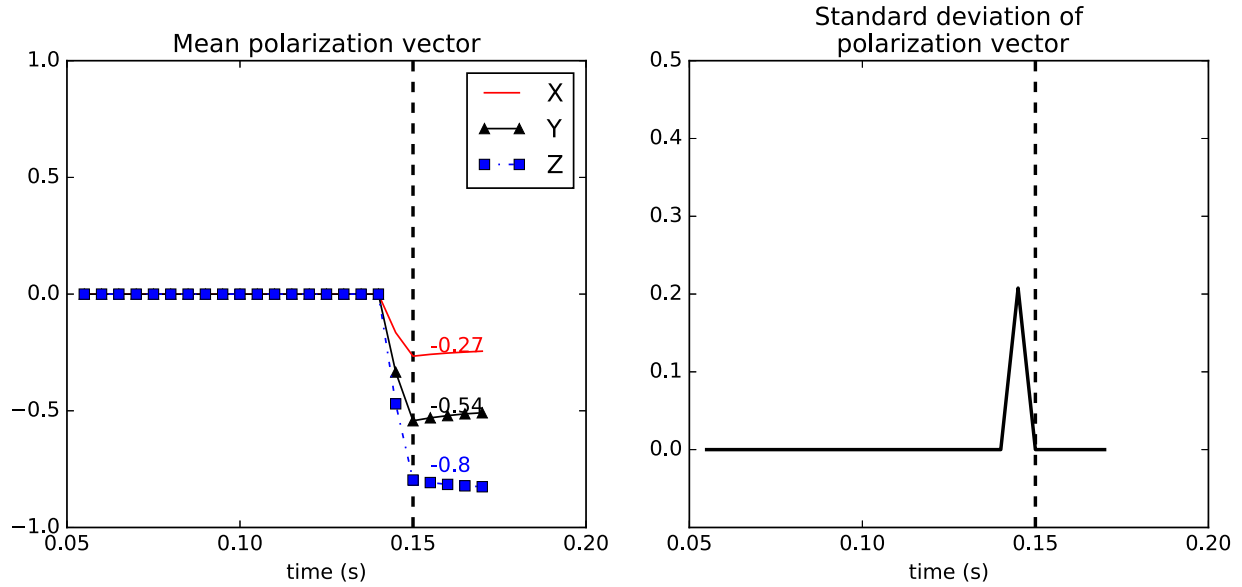
Figure 6. Three-component mean (left) and standard deviation (right) of polarization vectors as a function of time for denoising data. The polarization vector of this arrival in the data is selected to be $(-0.27, -0.54, -0.80)$.

$1, 2, \cdots N$. The standard deviation measures the variations of polarization vectors in the sliding window, given by

$$D(\mathbf{V}) = \frac{1}{N} \sum_{i=1}^{N} \left[(r_{x_i} - \bar{r}_x)^2 + (r_{y_i} - \bar{r}_y)^2 + (r_{z_i} - \bar{r}_z)^2 \right]^{1/2}, \tag{3}$$

where $r_{x_i}, r_{y_i}, r_{z_i}$ are the three components of the normalized polarization vector for a specific time in sliding window.

As the scanning window slides along the arrival range (light-grey box in Fig. 1), the mean and the standard deviation of polarization vector can be calculated for each sliding window, and shown as a function of time (Fig. 2). When the standard deviation versus time curve (dashed line marked in Fig. 2, right) reaches its first minimum after the first arrival time, We select the corresponding mean polarization vector (Fig. 2, left) as the polarization vector of first break, $(-0.27, -0.53, -0.80)$, while the central time of the corresponding sliding window (dark-grey slim window in Fig. 1) is regarded as the arrival time of the first-break (0.15 ms).

2.2 Denoising of first-break based on discrete wavelet transforms

Due to the relative small magnitudes of microseismic events, microseismic records are severely affected by background noise, which often makes it difficult to separate the first-breaks critical for event detection and polarization estimation. Discrete wavelet analysis has been suggested to suppress noise and extract frequency-domain features of microseismic records (Zhang *et al.* 2003; Bogiatzis & Ishii 2015; D'Auria *et al.* 2010), and proved to be an efficient method to separate the first-break waveform in multiple component records.

The discrete wavelet transform (DWT) transforms a signal $x(t)$ to the wavelet domain by passing it through a series of filters,

$$W_\psi(s, \tau) = \int_{-\infty}^{\infty} x(t) \psi^*_{s,\tau}(t) \mathrm{d}t \tag{4}$$

where the filters (e.g. mother wavelet) are given as

$$\psi_{s,\tau}(t) = \frac{1}{\sqrt{2^j}} \psi \left(\frac{t - k2^j}{2^j} \right), \tag{5}$$

and $s = 2^j$ and $\tau = k2^j$ are integers known as translation parameters. Suitable filters can be used with different translation parameters. For example, using high-pass filters can obtain detail coefficients, and using low-pass filters can get approximate coefficients.

To show how DWT can be used to denoise data, we first generate 3-C noisy microseismic data (Fig. 3) by adding Gaussian random noise with standard deviation of 5 per cent of maximum waveform amplitude to the synthetic data (in Fig. 1). The added noise makes the mean polarization vectors vary rapidly with time (Fig. 4, left), and the standard deviation of polarization vector irregular (Fig. 4, right). We employ Daubechies 4 wavelet to decompose the noisy data, and set to zero any detail coefficients below a threshold defined by the standard deviation of detail coefficients. We then use the approximation and new detail coefficients to reconstruct waveforms in which the background noise has been largely suppressed (Fig. 5). We also use a minimum amplitude threshold of 0.01 and set the motions of those sample below this threshold to be zero. We then apply polarization scanning method to the denoised waveforms, calculate the mean and standard deviation of polarization vectors, and select the polarization vector of this arrival (Fig. 6) as discussed in Section 2.1. In this case, the polarization vector
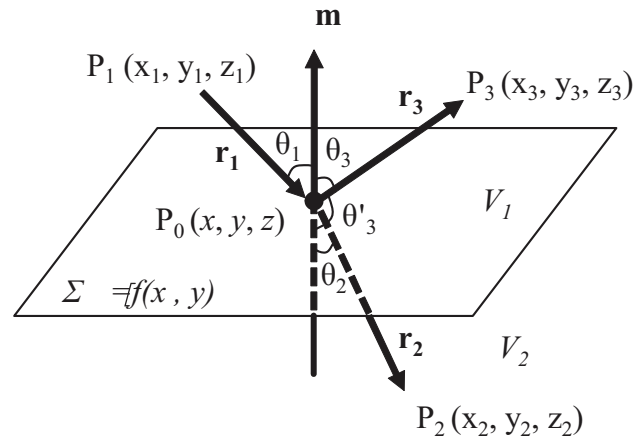
Figure 7. An interface Σ separating the upper layer with velocity V_1 and lower layer with velocity V_2. Seismic ray vector for the incident, transmitted and reflected waves at $\mathbf{P}_0$ are defined as $\mathbf{r}_1$, $\mathbf{r}_2$ and $\mathbf{r}_3$. The normal of the interface at $\mathbf{P}_0$ is parallel to the $\hat{\mathbf{m}}$ vector.

of this arrival in the denoised data is $(-0.27, -0.54, -0.80)$, which is very similar to the polarization vector determined for the noise-free waveforms in Fig. 1.

2.3 Corrections to apparent polarization vectors

As pointed out by Park & Ishii (2018), the polarization direction of the incident waves is not the same as the surface particle motion direction (also known as apparent polarization direction), and needs to be converted based on near-surface structures, because the first-arrival particle motion recorded on free surface is the superposition of incident P waves, the reflected P waves and reflected SV waves (Wiechert 1907, Nagano *et al.* 1989, Shearer 1999). If we assume the azimuth of the surface particle motion direction to be $\overline{\phi}$ and its angle from the vertical direction to be $\overline{\theta}$, then we have the remarkable result that $\overline{\theta}$ is twice the angle of reflected S ray vector from the vertical direction, ϕ_s, that is,

$$\overline{\theta} = 2\phi_s. \tag{6}$$

which can be used to calculate the S reflection angle ϕ_s. As the incident angle of P waves, θ, is related to the reflected S wave angle by the *Snell's Law*, that is,

$$\sin\theta = \frac{V_p}{V_s}\sin\phi_s, \tag{7}$$

the polarization angle of the incident P can be computed as

$$\theta = a\sin\left[\frac{V_p}{V_s}\sin\left(\frac{\overline{\theta}}{2}\right)\right]. \tag{8}$$

Apparently the surface V_p/V_s is needed to make this correction from the observed $\overline{\theta}$ to θ. For Poisson's solids, $V_p/V_s = \sqrt{3}$. Eq. (8) also indicates that if the surface V_p/V_s value is properly selected, then the observed surface motion $\overline{\theta}$ angle should never be larger than $2\sin^{-1}(V_s/V_p)$, and for Poisson's solids, this gives the maximum $\overline{\theta}$ angle of $\sim 70°$.

2.4 Vector-based seismic ray-tracing algorithm

Once the true polarization vectors of the incident waves are properly corrected from the apparent polarization vector (Section 2.3) which in turn is obtained from surface 3-C seismograms based on the polarization scanning method in Section 2.1, we can apply vector-based seismic ray-tracing algorithms to reconstruct the ray trajectories.

The incident P ray vector represents the direction of compressional waves arriving at a station, uniquely determined by the source and receiver positions, and background velocity structures. The reversibility of a P ray between source and receiver makes it possible to back-trace the incident P ray vector reverse in time from the station. When multiple P rays are back-traced from several stations, we can determine the source position and original time when P rays converged. For the sake of simplicity, we first derived the vector-based seismic ray-tracing formulae based on *Fermat's Principle* and then apply them to source localization in Section 2.5.

First let us consider seismic waves striking an interface Σ between an upper layer with velocity V_1 from a lower layer with velocity V_2 (Fig. 7). The geometry of the interface can be described by its elevation $z(x, y)$, and therefore the normal to the interface is parallel to $\hat{\mathbf{m}}$, is $(m_x, m_y, -1)$, where $m_x = \frac{\partial z}{\partial x}$ and $m_y = \frac{\partial z}{\partial x}$. We define the norm of $\mathbf{m}$ as m, such that $m^2 = m_x^2 + m_y^2 + 1$. Let us consider a seismic ray that leaves point $\mathbf{P}_1$ (with coordinates (x_1, y_1, z_1)) in the upper layer, penetrates through the interface at $\mathbf{P}_0$ (with coordinates (x, y, z)) and arrives

at point $\mathbf{P}_2$ (with coordinates (x_2, y_2, z_2)) in the lower layer. If the positions of $\mathbf{P}_1$ and $\mathbf{P}_2$ are fixed, then the actual ray path should correspond to the position of $\mathbf{P}_0$ that gives the minimum traveltime, defined as

$$T(x, y, z(x, y)) = \frac{\|\mathbf{P}_0 - \mathbf{P}_1\|}{V_1} + \frac{\|\mathbf{P}_2 - \mathbf{P}_0\|}{V_2}. \tag{9}$$

Based on Fermat's principle, the partial derivatives of this traveltime vanish as

$$\frac{\partial T}{\partial x} = \frac{\partial T}{\partial y} = 0. \tag{10}$$

Let us assume $\mathbf{r}_1 = (r_{1x}, r_{1y}, r_{1z})$, $\mathbf{r}_2 = (r_{2x}, r_{2y}, r_{2z})$, $\mathbf{r}_3 = (r_{3x}, r_{3y}, r_{3z})$, are the unit vectors in the incident, transmitted and reflected ray directions, and $\alpha = V_2/V_1$. Further derivations detailed in Appendix A give the explicit formulas to compute the three components of transmission vector $\mathbf{r}_2$ in terms of the incident ray vector and normal of the interface:

$$r_{2z} = \frac{\alpha[r_{1x}m_x + r_{1y}m_y + r_{1z}(m_x^2 + m_y^2)] - \text{sgn}(r_{1x}m_x + r_{1y}m_y - r_{1z})B^{1/2}}{m^2}, \tag{11}$$

$$r_{2x} = \alpha(r_{1x} + r_{1z}m_x) - r_{2z}m_x, \tag{12}$$

$$r_{2y} = \alpha(r_{1y} + r_{1z}m_y) - r_{2z}m_y, \tag{13}$$

where the parameter B is given by

$$B = m^2 - \alpha^2 \left[(r_{1y}m_x - r_{1x}m_y)^2 + (r_{1x} + r_{1z}m_x)^2 + (r_{1y} + r_{1z}m_y)^2\right]. \tag{14}$$

Similarly, the reflected ray vector is given by

$$r_{3z} = \frac{2(r_{1x}m_x + r_{1y}m_y) + r_{1z}(m_x^2 + m_y^2 - 1)}{m^2} \tag{15}$$

$$r_{3x} = r_{1x} + r_{1z}m_x - r_{3z}m_x \tag{16}$$

$$r_{3y} = r_{1y} + r_{1z}m_y - r_{3z}m_y. \tag{17}$$

As seismic ray trajectory is reversible, it is possible to trace back the ray path by reversing the incident vector at the station and find the intersection of the rays with the interface below. Eqs (11)–(17) can be used to directly calculate the direction of the reflected and transmitted ray vectors on/through the interface, which can be further used to build the next seismic ray segment until it reaches the next interface or as it approaches the source position.

2.5 Source localization based on polarization vectors

If the arrival time of first-break at ith receiver is measured to be T_i, the terminal point of P ray path at any time T ($T \le T_i$) can be obtained by back-tracing the seismic ray in reverse time from the receiver for $t = T_i - T$ which is the traveltime between the terminal point and receiver. We define the position of the ray terminal at T as $\mathbf{s}^i(T) = (x_i(T), y_i(T), z_i(T))$. With arrival times and polarization vectors measured at multiple stations, $\mathbf{x}_r^i$, $i = 1, , N$, a set of rays can be traced back from these receivers. Ideally, at the actual origin time of the event T_0, the terminal points on these reverse rays, $\mathbf{s}^i(T_0)$, $i = 1, , N$, should all coincide to give the source location, provided that the background model is accurately known. If ray terminals convergence to a point at time T, this point is considered the source location, and time T is regarded as the event origin time.

Theoretically, the source location and origin time can be determined by the intersection of reversed seismic rays from two receivers only. Of course in practice, owing to measurement errors and approximate background models, rays from two or more receivers may not converge to a single point. The time when all the ray terminals are the closest, quantified by the spread of the ray terminal points is selected as the origin time, and the mean position of the terminal points can be used as the source location. Beyond the selected origin time, these ray terminals start to diverge. We define the three components of the mean position of ray terminals for a given time T, $\mathbf{P}_r(T)$, as

$$\bar{x} = \frac{1}{N}\sum_{i=1}^{N} x_i, \quad \bar{y} = \frac{1}{N}\sum_{i=1}^{N} y_i, \quad \bar{z} = \frac{1}{N}\sum_{i=1}^{N} z_i \tag{18}$$

and the standard deviation (i.e. spread) of ray terminals as

$$D(\mathbf{P}_r(T)) = \frac{1}{N}\left\{\sum_{i=1}^{N}[(x_i - \bar{x})^2 + (y_i - \bar{y})^2 + (z_i - \bar{z})^2]\right\}^{1/2}. \tag{19}$$

We regarded $\mathbf{P}_r(T)$ as the real source location and the time T as the origin time when $D(\mathbf{P}_r(T))$ reaches the minimum.

Table 1. Forwarding model.

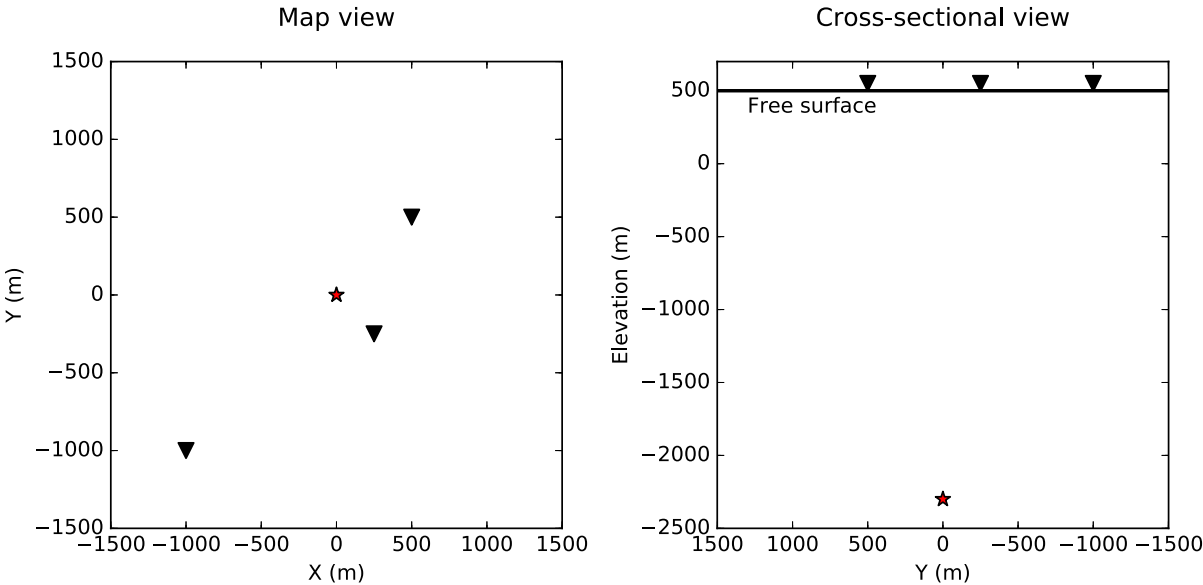| Layer No.	Interface elevation function (m)	V_p (m s^{-1})
1	$z = 500$	3200
2	$z = 100 + 10[\sin(0.0005x) + \cos(0.0001y)]$	3250
3	$z = -200 + 10[\sin(0.0001x) + \cos(0.0004y)]$	3300
4	$z = -500 + 10[\sin(0.0001x) + \cos(0.0003y)]$	3350
5	$z = -800 + 10[\cos(0.0003x) + \cos(0.0001y)]$	3400
6	$z = -1100 + 10[\sin(0.0001x) + \cos(0.0005y)]$	3450
7	$z = -1400 + 10[\sin(0.0003x) + \cos(0.0001y)]$	3500
8	$z = -1700 + 10[\sin(0.0001x) + \cos(0.0005y)]$	3550
9	$z = -2000 + 10[\sin(0.0001x) + \cos(0.0005y)]$	3600

Figure 8. Left: Three stations are deployed on the surface at (500.0, 500.0, 500.0) m, (− 1000.0, −1000.0, 500.0) m, (250.0, −250.0, 500.0) m, respectively. The source (the star) is located at position (− 1000.0, −1000.0, −2300.0) m. Right: The vertical cross-section view of source and stations.

Table 2. Modelling results of traveltimes and polarization directions of first arrivals for the three stations (shown in Fig. 8) based on SIRT.

| Geophone No.	Location (m)			Traveltime (s)	Polarization vector		
	x	y	z		r_x	r_y	r_z
1	500.0	500.0	500.0	0.85	−0.13	−0.13	−0.98
2	−1000.0	−1000.0	500.0	0.93	0.25	0.25	−0.94
3	250.0	−250.0	500.0	0.83	−0.07	0.07	−0.99

As the geophone array with multiple stations are widely deployed in microseismic monitoring, with varying geometry such as the Star Array, patch array, and large N array (Duncan & Eisner 2010; Caffagni *et al.* 2016; Roux et al. 2014; Li *et al.* 2017), the reliability and accuracy of source locating can be improved by using a large number of seismic rays back-traced from multiple stations to the actual source position.

# 3 SOURCE LOCALIZATION BASED ON RTRTM

3.1 Synthetic examples

In this synthetic example, we first define a complex three-dimensional layered background model with nine velocity interfaces. The *P* velocity for each layer between two neighbouring interfaces is constant as given by Table 1. The top interface with constant elevation at 500.0 m is flat and regarded as the surface. The second undulating sinusoidal interfaces has an average elevation at 100 m. The next seven interfaces are sinusoidal functions with average depths at 200, 500, 800, 1100, 1400, 1700 and 2000 m, with interface undulations all around 10 m.

As shown in Fig. 8, for a source (shown as a star) located at 2300 m depth, three surface stations (shown as triangles) are used for source localization. To test the RTRTM, we first calculate the traveltime and polarity vector of the incident *P* wave at these three stations for the 3D background model (shown in Table 2) using the segmentally iterative ray tracing (SIRT; Gao *et al.* 2002, 2007, 2008; Xu *et al.* 2006, 2010,
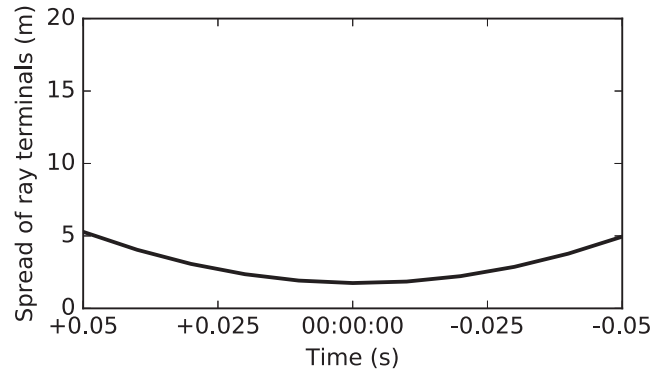
Figure 9. The spread of three back-traced terminal points as a function of time. It reaches the minimum at time $T = 0$, which can be regarded as the original time. As the T goes below 0, ray terminals start to diverge.
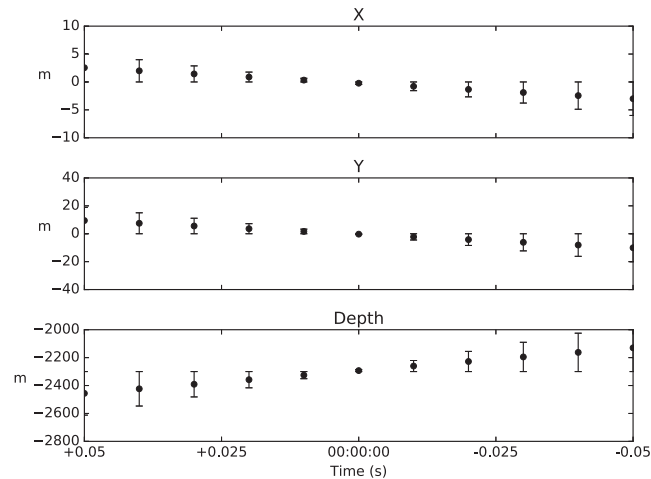
Figure 10. The mean ray terminal positions (X, Y and depth) as a function of time T, while the error bars indicate the difference between the mean terminal position and the assumed source position. The error reaches minimum at time $T = 0$, which is the same as the true origin time.

2014). SIRT is a ray bending method for two-point ray tracing by adjusting the intersection points of seismic ray and interfaces iteratively to get the minimum traveltime path. We assume the origin time of the source is at zero time. The computed arrival times of the first break recorded at these three receivers T_i, $i = 1, 2, 3$ are listed in Table 2. For the synthetic data in this section, no reflected and transmitted wave are simulated for the first arrival (Section 3.1), and do not distinguish between apparent and true polarization directions.

We back trace the three first-break ray path in reverse time and calculate the terminal positions at time T, where $T_i - T$ represents the traveltime between the terminal point and receiver. As the seismic rays are back-traced in reverse time and when all ray terminal points converging to a point or the spread (eq. 19) of all ray terminals reaches minimum, the corresponding T becomes the event origin time and the mean position of ray terminals (eq. 18) is regarded as the source location.

For this case, the three back-traced rays have their terminal points converge at time 00: 00: 00 (Fig. 9) when the average distance reach to the minimum. The initial time is selected at time $T = 0$, which is the same as the origin time we initially assumed. The mean position of three terminals is $(0.09, -0.2, -2300.8)$ m, very close to the original source position at $(0, 0, -2300)$ m. Also as shown in Fig. 10, the mean terminal position gradually approaches the true source location and its error reaches minimum at time $T = 0$.

We perform another numerical experiment with two perpendicular surface geophone arrays with the same source location and background velocity model (Table 1). The receiver arrays consist of 17 seismic stations (Fig. 11), 10 of which deployed along x direction, and 8 along the y direction. The two arrays share a common receiver located at the intersection of these two arrays. We still set a source at $(-1000.0, -1000.0, -2300.0)$ m and assume the origin time to be at zero time. We calculate the traveltimes and polarity vectors of the incident P rays at all receivers based on SIRT, as shown in Table 3.

Using the polarization of incident P rays at all 17 receivers, we back trace these ray paths reverse in time, and calculate the ray terminal points at a set of time T. As shown in Fig. 12, the spread of ray terminal points converges gradually with time close $T = 0$, and then increases with decreasing T. And at $T = 0$, we select the mean terminal position at $(-1000.54, -1002.41, -2304.56)$ m as the source location (Fig. 13). The distance between the back-traced and true source positions is around 5 m, tiny compared to the average source-receiver distances of ~3000 m.
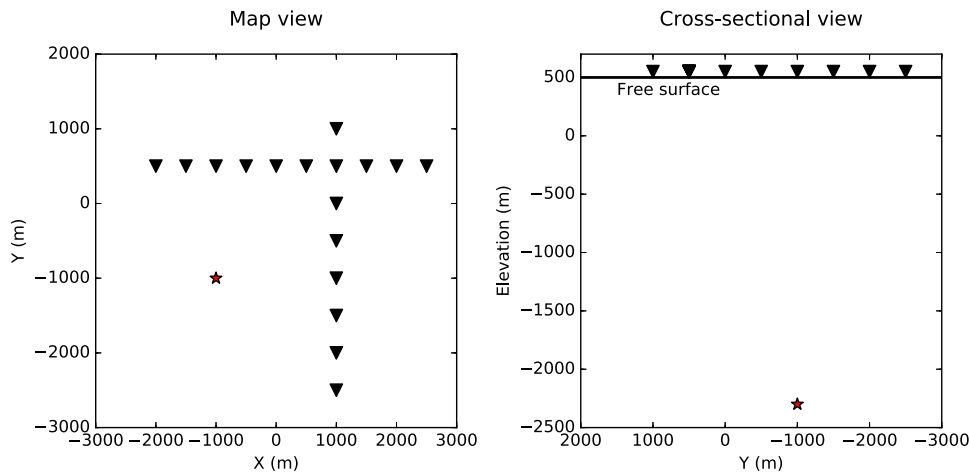
Figure 11. Left: The receiver arrays consist of 17 seismic stations, 10 of which deployed along *x* direction, 8 along the *y* direction. The two arrays share a common receiver located on the intersection of geophone arrays. Right: The vertical cross-section view of source and stations. The source is at (− 1000, −1000, −2300) m.

Table 3. The traveltimes and polarization vectors from forward modelling based on SIRT method for the source–receiver geometry shown in Fig. 11.

| Geophone No.	Location (m)			Traveltime (s)	Polarization vector		
	x	y	z		r_x	r_y	r_z
1	1000.0	1000.0	500.0	1.17	−0.43	−0.43	−0.79
2	1000.0	500.0	500.0	1.11	−0.45	−0.34	−0.83
3	1000.0	0.0	500.0	1.06	−0.46	−0.23	−0.86
4	1000.0	−500.0	500.0	1.03	−0.47	−0.12	−0.87
5	1000.0	−1000.0	500.0	1.02	−0.48	0.00	−0.88
6	1000.0	−1500.0	500.0	1.03	−0.47	0.12	−0.87
7	1000.0	−2000.0	500.0	1.06	−0.46	0.23	−0.86
8	1000.0	−2500.0	500.0	1.11	−0.45	0.34	−0.83
9	−2000.0	500.0	500.0	0.98	0.24	−0.36	−0.90
10	−1500.0	500.0	500.0	0.95	0.12	−0.37	−0.92
11	−1000.0	500.0	500.0	0.94	0.00	−0.37	−0.93
12	−500.0	500.0	500.0	0.95	−0.12	−0.37	−0.92
13	0.0	500.0	500.0	0.98	−0.24	−0.36	−0.90
14	500.0	500.0	500.0	1.04	−0.35	−0.35	−0.87
15	1500.0	500.0	500.0	1.19	−0.53	−0.32	−0.78
16	2000.0	500.0	500.0	1.29	−0.60	−0.30	−0.74
17	2500.0	500.0	500.0	1.39	−0.66	−0.28	−0.69
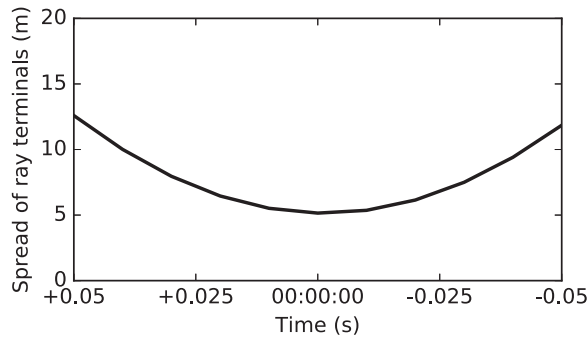
Figure 12. The average distance between 17 terminal points and their mean point converges at the real time 00: 00: 00, as the 17 ray trajectories of first-break tracing reverse time. The time 00: 00: 00 is regarded as the original time when the average distance reaches to the minimum. As the real time moves away from the initial time, seismic rays diverge gradually. .
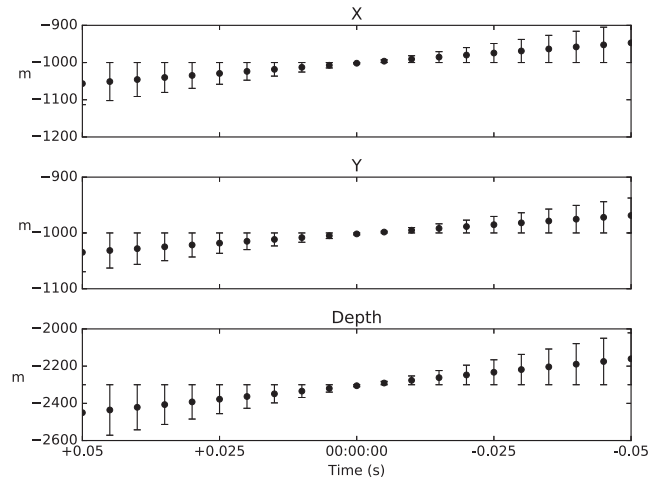
Figure 13. Error of the X, Y and depth between the mean terminal point and the assumed source position as seismic ray back tracing reverse time. The mean ray terminal reaches to the assumed source at the real time 00: 00: 00, and that time equals to the origin time we assumed.

Table 4. The coordinates of the four seismic stations shown in Fig. 14, the azimuth of incident P direction (PMD-$\overline{\phi}$), the apparent incident angle of particle motion direction (PMD-$\overline{\theta}$), and the corrected incident angle based on IASP91 model (IASP91) and in SJA model (SJA).

|	Station		PMD		Corrected incident angle	
Name	Lat. (°)	Lon. (°)	$\overline{\phi}$ (°)	$\overline{\theta}$ (°)	IASP91 (°)	SJA (°)
DH	34.51	118.77	259.09	52.54	49.82	50.06
GUY	34.31	119.24	238.14	41.43	37.63	37.78
LYG	34.64	119.24	298.22	49.35	46.10	46.31
XW	34.50	119.54	154.22	6.47	5.59	5.61
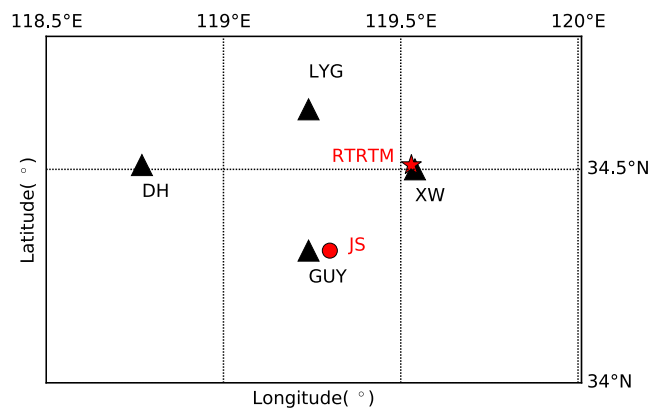
Figure 14. The locations of four seismic station (black triangles) operated by the Seismological Bureau of Jiangsu Province, China. The red circle represents the epicentral location in the earthquake catalogue while the red star indicates the epicentral location determined by RTRTM based on the incident vector of P rays.

3.2 Field data

Now we investigate the feasibility of applying RTRTM to actual field data. For a $M_b = 1.6$ event occurred at 13: 52: 30 (GMT Time) on December 11th, 2016 at Lianyungang, Jiangsu, seismic arrivals were observed on four 3-C high broad-band (sampling rate at 100 Hz) stations (listed in Table 4) in as shown in Fig.14. We first use Daubechies 2 wavelet to decompose the 3-C recordings, set to zero any detailed coefficients below a threshold defined by the standard deviation of detail coefficients, and then reconstruct denoised waveforms (the solid curves shown in Fig. 15). With the apparent polarization direction determined from polarization scanning method, a correction is applied to obtain the true polarization direction of the incident P waves based on near-surface V_p and V_s velocities. In this study, we use 1.726 for IASP91 model, and assume $V_p/V_s = \sqrt{3}$ for other models.

We select part of data containing the first break (light-grey time window in Fig. 15) to estimate the particle motion directions. The length of scanning window is selected to be 40 ms (dark-grey time window in Fig. 15), and the sliding step is 10 ms. The amplitudes of 3-C data within the scanning windows are used to estimate the mean (Fig. 16, left) and corresponding standard deviation (Fig. 16, right) of apparent polarization vectors. The standard deviation goes down as the particle motion vectors in the sliding window become stable and tend towards
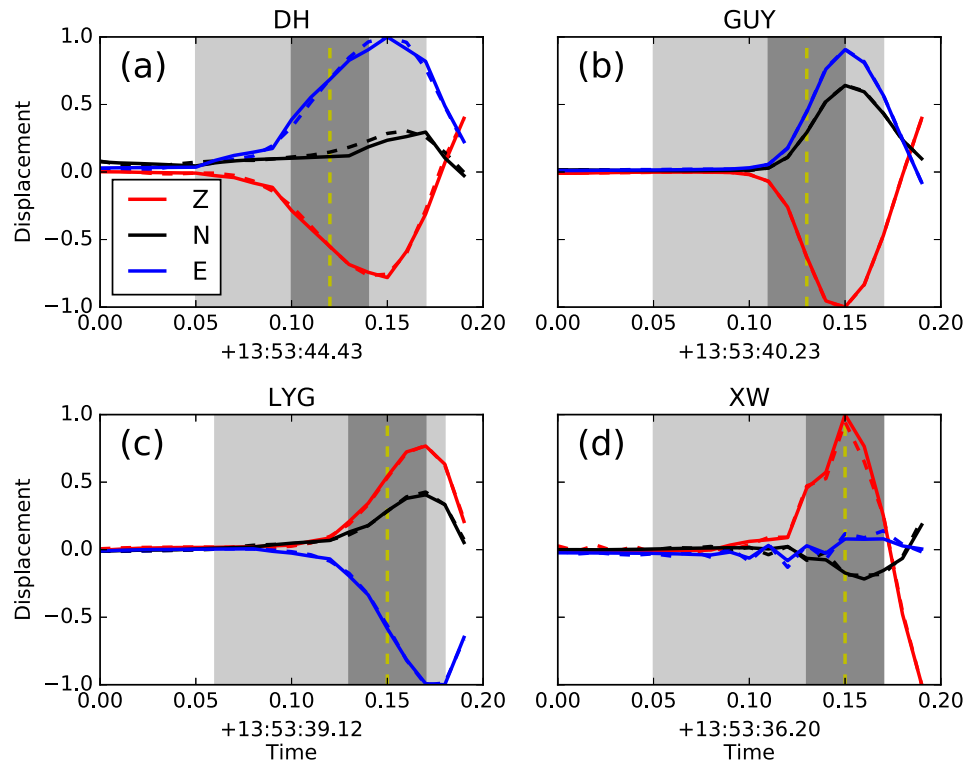
Figure 15. Three-component seismogram (dashed curves), denoised waveforms based on DWT (solid curves), selected polarization scanning time range (light-grey box), scanning window (dark-grey box) and the time at which the particle motion directions are selected (yellow dashed lines) for stations DH (a), GUY (b), LYG (c) and XW (d).

the same direction. Therefore, the standard deviation of the apparent polarization vector can be used as a first-break picker by selecting the time of first minimum in standard deviation with non-zero amplitude waveforms as the arrival time of incident *P* wave (yellow vertical lines in Fig. 16), and the corresponding displacement vector as the apparent polarization direction.

For example, for station DH (Fig. 16a, right), the minimum value of standard deviation appears at time 13: 53: 44.55 which indicates that the particle motion vector is most consistent around that time with a mean vector of (0.77, 0.15, −0.60), as shown in Fig. 16 a (left). It is also reassuring to observe that the mean vector becomes more consistent after time 13: 53: 44.55 (Fig. 16a, left). The mean vectors for GUY, LYG and XW can be determined in a similar fashion. These results are presented as the azimuth and incident angle of particle motion direction, listed in Table 4. Typically, the mean polarization vectors in the scanning windows may become more consistent due to the arrival of compressional waves generated from the continuously propagated rupture tip.The propagating rupture can still be regarded as a point source because the length of rupture is usually far smaller than the distance between the source and station. The seismic rays coming from the moving 'point source' have similar polarizations when arriving at the same station and results in similar particle motions on the surface.

We first use the *IASP91* model (Kennett 1991; Trabant *et al.* 2012) as the background model for source localization. The effect of velocity model on RTRTM will be further discussed in Section 4. From the estimated particle motion directions (PMD), we calculate the incident direction of *P* waves based on eqs (6)–(8) using the surface $V_p/V_s = 1.726$ for *IASP91*, and the results are shown in Table 4, IASP91.

These *P* incident vectors are further used to locate the source based on RTRTM, and give the source hypocentre at 34.51° N, 119.53° E, 28.66 km depth (the red star in Fig. 14) and the event origin time around 13: 53: 31.85 (GMT). Note that compared to the event parameters from the network catalogue, our origin time is delayed by almost 2 seconds, and the event epicentre is shifted to northeast by at least 50 km towards the station XW. It can be confirmed directly from the corrected incident angle for station XW (Table 4), which is as small as 5.59°. The fact that the incident *P* ray arrives almost vertically indicates that the source is almost right below XW.

We have also tested that using the particle motion directly (Table 4, PMD) without applying the incident angle correction as in eqs (6)–(8) before the ray tracing in RTRTM, the located source based on *IASP91* model has epicentre at 34.52° N, 119.55° E, less than 3 km away from the epicentre determined earlier. However, the located source depth is at 31.89 km, 3.2 km deeper than the depth determined by the corrected incident vectors (Table 4, IASP91) based on IASP91 model. Therefore not applying incident angle correction may result in significant source depth errors.
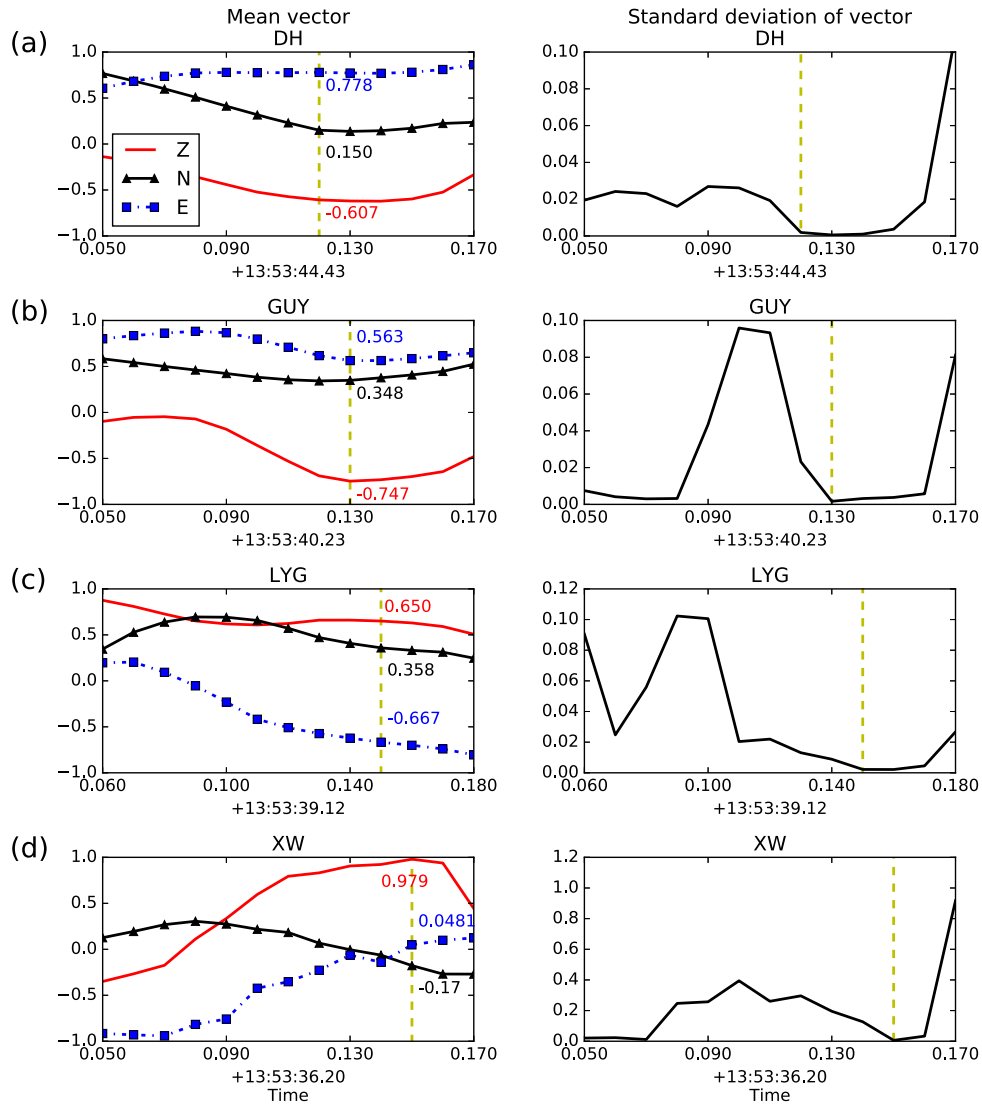
Figure 16. The mean (left) and standard deviation (right) of surface motion direction for sliding windows for four stations, DH(a), GUY(b), LYG(c) and XW(d). The yellow lines mark the selected mean vector when the standard deviation of the vectors first reaches the minimum.
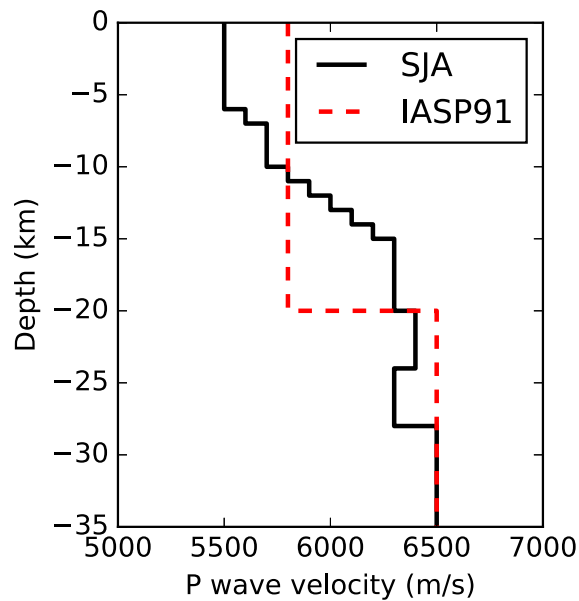
Figure 17. The V_p velocity models used for source localization. V_s is assumed to be $1/\sqrt{3}$ of V_p for model *SJA*, and $V_s = 3.5\,\mathrm{km\,s^{-1}}$ at near surface for IASP91.
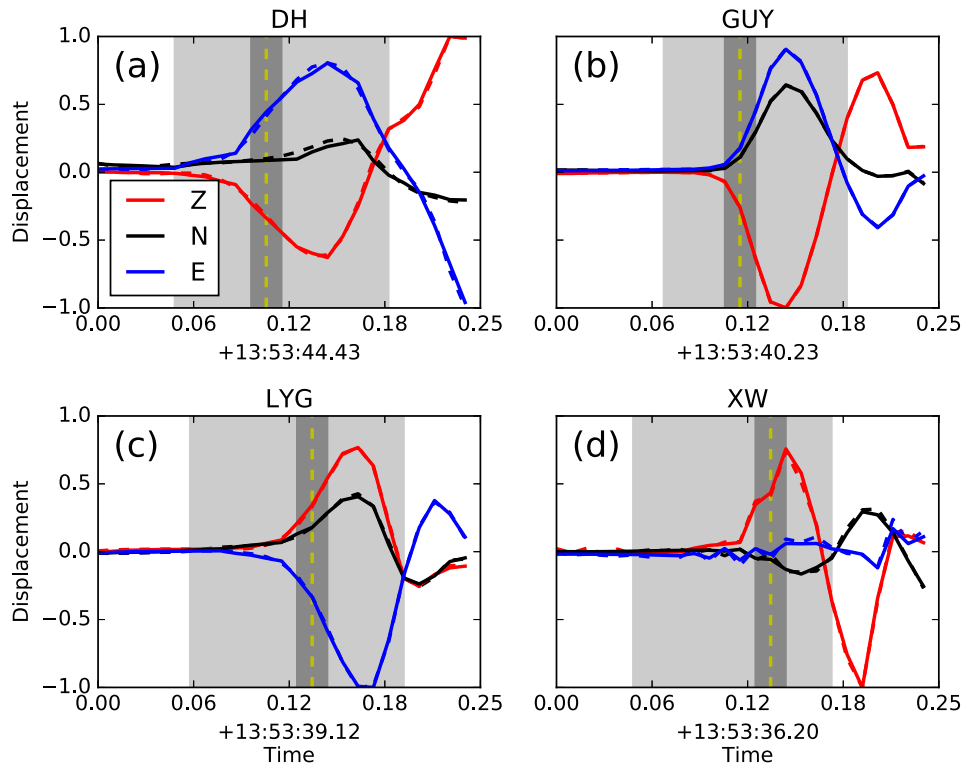
Figure 18. Same as Fig. 15 except the scanning window length has been shortened from 40 to 20 ms.

4 DISCUSSION

4.1 Reliability of particle motion direction estimation based on polarization scanning method

Using the field data example, we investigate the reliability of the polarization scanning method by changing the length of the sliding window from 40 ms to 20 ms (dark-grey range in Fig. 18) and keeping the sliding step length at 10 ms. The scanning results for the four stations are shown in Fig. 19. We select the apparent polarization to be associated with the time when the standard deviation of particle motion vectors reaches minimum (marked with yellow dashed line in the right column of Fig. 19). The scanning results for station DH (Fig. 19a) shows that the apparent polarization vector is $(0.78, 0.18, -0.58)$, similar to the results obtained in Fig. 16(a), and the mean polarization vector is consistent for almost 50 ms after the standard deviation curve reaches the minimum. Similar conclusion can be drawn for station GUY and LYG, except the mean polarization vector is only consistent for 40 ms (GUY) and 30 ms (LYG) after the standard deviations reaches the minimum. For station XW, the selected mean polarization vector is $(0.008, -0.1, 0.989)$, close to that in Fig. 16(d). However, it is much less well constrained than the other three stations because the mean vector is only persistent for about 15 ms after the standard deviations reaches the minimum.

We also compare our particle motion direction estimation to those calculated based on PCA. We select the same first-arrival time range (light-grey windows in Fig. 18) to perform PCA and show results of particle motion directions at the four stations in Table 5 and Fig. 20, in comparison to the results based on polarization scanning methods. Clearly the apparent polarization vectors obtained by polarization scanning method is consistent with the general displacement direction and also close to the results by PCA.

4.2 The effect of background velocity model on RTRTM

The effect of background velocity model for source localization based on RTRTM is two-fold. First, when we use eqs (6)–(8) to calculate the incident vector of P waves from the measured surface particle motion directions, the near surface V_p/V_s ratio is needed. For example, this ratio is 1.726 at the near surface for *IASP91* model, and we assume the standard $V_p/V_s = \sqrt{3} \approx 1.732$ value in another model, *SJA* (see Fig. 17). For the field data case, the difference in P incident angles as a result of this difference is generally less than 1° (shown in Table 4). This error is relative minor compared to those resulted from not applying incident angle corrections. Of course, when the surface V_p/V_s values show significant deviation from the standard value, this error can become more important.

In practice, the near surface structures can be obtained from geophysical methods such as reflection seismic survey and near-surface well logging.

Now we explore the effect of different background velocity structures to ray tracing in RTRTM for source localization. We first build a 1D P-velocity model based on a recent tomographic study for this area (Zhen *et al.* 2016), named *SJA*, with eleven horizontal interfaces
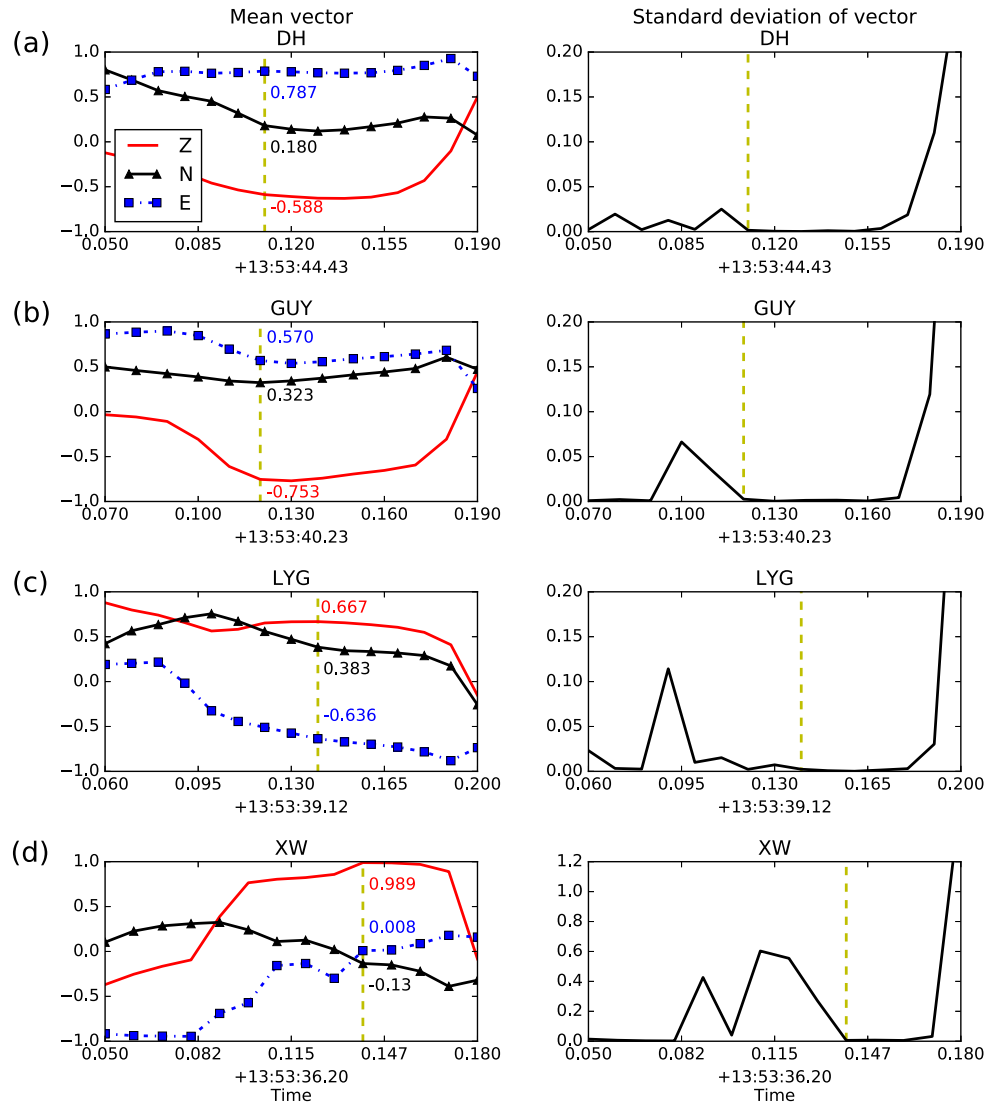
Figure 19. Same as Fig. 16 except the scanning window length has been shortened from 40 to 20 ms.

Table 5. Particle motion directions (PMD) estimated based on PCA and polarization scanning method with different scanning window length.

Station	PCA		PMD (40 ms)		PMD (20 ms)	
	$\overline{\phi}$ (°)	$\overline{\theta}$ (°)	$\overline{\phi}$ (°)	$\overline{\theta}$ (°)	$\overline{\phi}$ (°)	$\overline{\theta}$ (°)
DH	259.29	48.77	259.09	52.54	257.12	53.93
GUY	238.45	42.11	238.14	41.43	240.46	41.03
LYG	294.03	53.94	298.22	49.35	301.06	48.06
XW	166.76	10.10	154.22	6.47	176.48	7.50

(Fig. 17), and velocity within each layer constant. The *P* velocity increases gradually from 5.5 km s^{-1} at 5 km depth to 6.5 km s^{-1} at 30 km depth. Clearly, *SJA* model is much more refined above 30 km compared to *IASP91* model. The incident ray vectors of *P* waves for *SJA* model are shown in Table 4, SJA. With these incident ray vectors, we locate the source back to 34.51°N, 119.53°E, and 33.45 km depth, and the event original time to 13: 53: 31.35 (GMT). All source parameters are consistent with those based on *IASP91* in Section 3.2 except the depth is moved 4.79 km deeper. This shows that depth is much less well constrained in source localization, which may need to be further improved with increased station coverage.

5 CONCLUSIONS

We present an RTRTM to locate microseismic source position. The RTRTM estimates the particle motion directions and arrival times at stations based on polarization scanning method, corrects them for the polarization of incident *P* waves, and back-traces of these ray vectors to select the optimal source position and event origin time when all rays converged. Our synthetic tests and field-data examples shows the
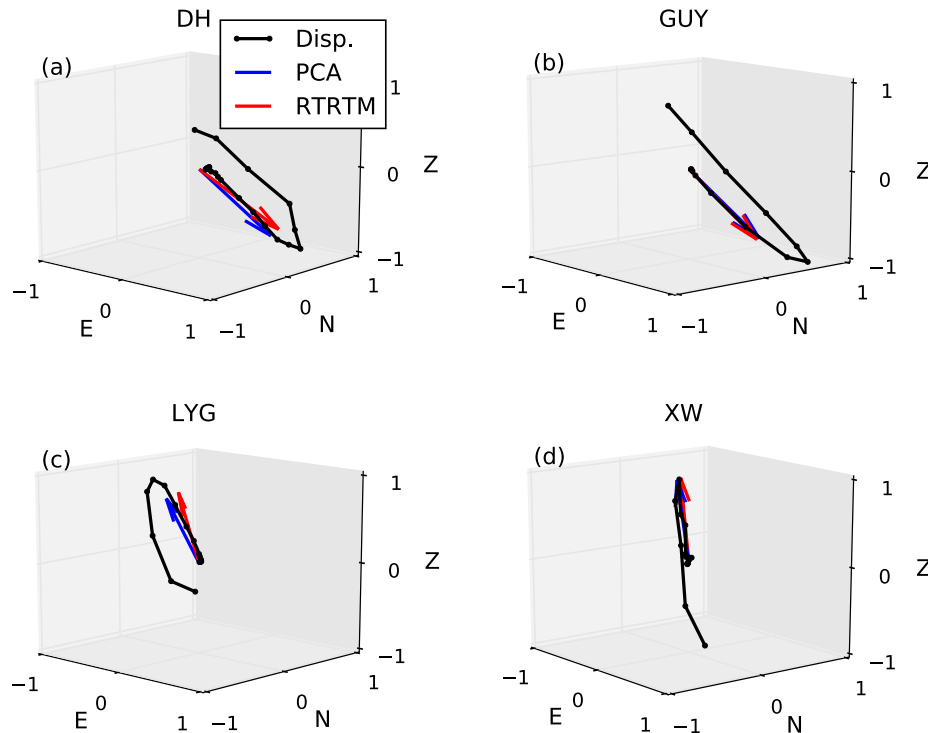
Figure 20. The three-component particle displacement (black lines), and the best particle motion directions obtained by Principal Component Analysis (blue arrows) and the polarization estimation method (red arrows) for four stations: DH(a), GUY(b), LYG(c) and XW(d).

great promise of using 3-C recordings for accurate source parameter estimation, and our methods can be readily applied to microseismic monitoring scenarios when 3-C recordings are available. The comparison between polarization estimations by polarization scanning and the PCA for field data shows great consistency. The background velocity model can affect the source localization by the surface V_p/V_s values used in incident angle corrections and the backward ray tracing. Therefore more accurate velocity structures are always desirable in reducing the uncertainty in source locations and may need to be obtained through other geophysical methods, such as well-logging and reflection seismic survey.

REFERENCES

Akaike, H., 1998. *Information Theory and an Extension of the Maximum Likelihood Principle,* Springer, pp. 199–213.

Artman, B., Podladtchikov, I. & Witten, B., 2010. Source location using time-reverse imaging, *Geophys. Prospect.,* **58,** 861–873.

Bai, C., Huang, G. & Zhao, R., 2010. 2-D/3-D irregular shortest-path ray tracing for multiple arrivals and its applications, *Geophys. J. Int.,* **183,** 1596–1612.

Bayer, B., Kind, R., Hoffmann, M., Yuan, X. & Meier, T., 2012. Tracking unilateral earthquake rupture by P-wave polarization analysis, *Geophys. J. Int.,* **188,** 1141–1153.

Bogiatzis, P. & Ishii, M., 2015. Continuous wavelet decomposition algorithms for automatic detection of compressional- and shear-wave arrival times, *Bull. seism. Soc. Am.,* **105,** 1628–1641.

Buland, R. & Chapman, C.H., 1983. The computation of seismic travel times, *Bull. seism. Soc. Am.,* **73,** 1271–1302.

Bulant, P., 1996. Two-point ray tracing in 3D, *Pure appl. Geophys.,* **148,** 421–447.

Caffagni, E., Eaton, D.W., Jones, J.P. & van der Baan, M., 2016. Detection and analysis of microseismic events using a Matched Filtering Algorithm (MFA), *Geophys. J. Int.,* **206** (8):644–658.

Cerveny, V., 2005. *Seismic Ray Theory,* Cambridge Univ. Press.

D'Auria, L., Giudicepietro, F., Martini, M., Orazi, M., Peluso, R. & Scarpato, G., 2010. Polarization analysis in the discrete wavelet domain: an application to volcano seismology, *Bull. seism. Soc. Am.,* **100,** 670–683.

Duncan, P. M. & Eisner, L., 2010. Reservoir characterization using surface microseismic monitoring, *Geophysics,* **75,** 75A139–75A146.

Ellsworth, W.L., 2013. Injection-induced earthquakes, *Science,* **341,**

Folesky, J., Kummerow, J. & Shapiro, S.A., 2015. Microseismic rupture propagation imaging, *Geophysics,* **80,** WC107–WC115.

Galiana-Merino, J.J., Rosa-Herranz, J., Giner, J., Molina, S. & Botella, F., 2003. De-noising of short-period seismograms by wavelet packet transform, *Bull. seism. Soc. Am.,* **93,** 2554–2562.

Galiana-Merino, J.J., Rosa-Herranz, J., Járegui, P., Molina, S. & Giner, J., 2007. Wavelet transform methods for azimuth estimation in local three-component seismograms, *Bull. seism. Soc. Am.,* **97,** 793–803.

Gambino, S., Mostaccio, A., Patanè, D., Scarfi, L. & Ursino, A., 2004. High-precision locations of the microseismicity preceding the 2002-2003 Mt. Etna eruption, *Geophys. Res. Lett.,* **31,** L18604, doi:10.1029/2004GL020499.

Gao, E., Uk, H. & Teng, J., 2007. Fast ray tracing method in 3-D structure and its proof of positive definiteness, *J. Cent. South Univ. Technol.,* **14,** 100–103.

Gao, E., Xu, G., Jiang, X., Luo, K. & Liu, T., 2002. Iterative ray-tracing method segment by segment under 3-D construction, *OGP,* **37,** 11–16.

Gao, E., Zhang, A., Uk, H., Song, S. & Zhai, Y., 2008. Fast algorithm and numerical simulation for ray-tracing in 3D structure, *J. Cent. South Univ. Technol.,* **15,** 901–905.

Goertz-Allmann, B.P., Kühn, D., Oye, V., Bohloli, B. & Aker, E., 2014. Combining microseismic and geomechanical observations to interpret storage integrity at the In Salah CCS site, *Geophys. J. Int.,* **198,** 447–461.

Grigoli, F., Cesca, S., Amoroso, O., Emolo, A., Zollo, A. & Dahm, T., 2014. Automated seismic event location by waveform coherence analysis, *Geophys. J. Int.,* **196,** 1742–1753.

Haldorsen, J.B., Brooks, N.J. & Milenkovic, M., 2013. Locating microseismic sources using migration-based deconvolution, *Geophysics,* **78,** KS73–KS84.

Jansky, J., Plicka, V. & Eisner, L., 2010. Feasibility of joint 1D velocity model and event location inversion by the Neighbourhood algorithm, *Geophys. Prospect.,* **58,** 229–234.

Jones, G.A., Kendall, J.M., Bastow, I.D. & Raymer, D.G., 2014. Locating microseismic events using borehole data, *Geophys. Prospect.,* **62,** 34–49.

Jurkevics, A., 1988. Polarization analysis of three-component array data, *Bull. seism. Soc. Am.,* **78,** 1725–1743.

Kennett, B.L.N., 1991. *IASPEI 1991 Seismological Tables, Bibliotech,* Canberra, Australia, 167.

King, A. & Talebi, S., 2007. Anisotropy effects on microseismic event location, *Pure appl. Geophys.,* **164,** 2141–2156.

Larmat, C., Tromp, J., Liu, Q. & Montagner, J.P., 2008. Time reversal location of glacial earthquakes, *J. geophys. Res.,* **113,** 1–9.

Li, X., Shang, X., Morales-Esteban, A. & Wang, Z., 2017. Identifying P phase arrival of weak events: the Akaike information criterion picking application based on the empirical mode decomposition, *Comput. Geosci.,* **100,** 57–66.

Maxwell, S.C., Rutledge, J., Jones, R. & Fehler, M., 2010. Petroleum reservoir characterization using downhole microseismic monitoring, *Geophysics,* **75,** 75A129–75A137.

Miksat, J., Müller, T.M. & Wenzel, F., 2008. Simulating three-dimensional seismograms in 2.5-dimensional structures by combining two-dimensional finite difference modelling and ray tracing, *Geophys. J. Int.,* **174,** 309–315.

Moriya, H., Nagano, K. & Niitsuma, H., 1994. Precise source location of AE doublets by spectral matrix analysis of triaxial hodogram, *Geophysics,* **59,** 36–45.

Nagano, K., Niitsuma, H. & Chubachi, N., 1989. Automatic algorithm for triaxial hodogram source location in downhole acoustic emission measurement, *Geophysics,* **54,** 508–513.

Hirabayashi, N., 2016. Real-time event location using model-based estimation of arrival times and back azimuths of seismic phases. *Geophysics,* **81,** KS25–KS40.

Magotra, N., Ahmed, N. & Chael, E., 1989. Single-station seismic event detection and location, *IEEE Trans. Geosci. Remote Sens.,* **27,** 15–23.

O'Brien, G. S., Lokmer, I., De Barros, L., Bean, C. J., Saccorotti, G., Metaxian, J. P. & Patane, D., 2011. Time reverse location of seismic long-period events recorded on Mt Etna, *Geophys. J. Int.,* **184,** 452–462.

Oye, V. & Roth, M., 2003. Automated seismic event location for hydrocarbon reservoirs, *Comput. Geosci.,* **29,** 851–863.

Park, S. & Ishii, M., 2018. Near-Surface Compressional and Shear Wave Speeds Constrained by Body-Wave Polarisation Analysis. *Geophys. J. Int.,* **213,** 1559–1571.

Pearson, K., 1901. On lines and planes of closest fit to systems of points in space. *Phil. Mag. J.,* **2,** 559–572.

Price, D., Angus, D., Chambers, K. & Jones, G., 2015. Surface microseismic imaging in the presence of high-velocity lithologic layers, *Geophysics,* **80,** WC117–WC131.

Roux, P.F., Kostadinovic, J., Bardainne, T., Rebel, E., Chmiel, M., Van Parys, M., Macault, R. & .Pignot, L, 2014. Increasing the accuracy of microseismic monitoring using surface patch arrays and a novel processing approach, *First Break,* **32** (8):95–101.

Saari, J., 1991. Automated phase picker and source location algorithm for local distances using a single three-component seismic station, *Tectonophysics,* **189,** 307–315.

Sethian, J.A. & Popovici, A.M., 1999. 3-D traveltime computation using the fast marching method, *Geophysics,* **64,** 516–523.

Shearer, P.M., 1999, *Introduction to Seismology,* Cambridge Univ. Press, p. 260

Shi, Y. & Wang, W.H., 2012. Surface-related multiple suppression approach by combining wave equation prediction and hyperbolic Radon transform, *Chin. J. Geophys.,* **55,** 3115–3125.

Tan, Y., Li, L., Zhang, X. & He, C., 2017. An improved method for microseismic source location based on grid search, *Chin. J. Geophys.,* **60,** 293–304.

Trabant, C., Hutko, A.R., Bahavar, M., Karstens, R., Ahern, T. & Aster, R., 2012. Data Products at the IRIS DMC: Stepping Stones for Research and Other Applications, *Seismol. Res. Lett.,* **83,** 846–854.

Um, J. & Thurber, C., 1987. Fast algorithm for two-point seismic ray tracing. *Bull. seism. Soc. Am.*, **77,** 972–986.

Wiechert, E., 1907. Uber Erdbebenwellen. Part I: Theoretisches "uber die" Ausbreitung der Erdbebenwellen, Nachrichten von der K. Gesellschaft der Wissenschaften zu Gottingen, *Math. Phys. Klasse,* 415–529.

Vidale, J.E., 1986, Complex polarization analysis of particle motion, *Bull. seism. Soc. Am.*, **76,** 1393–1405.

Xu, T., Li, F., Wu, Z., Wu, C., Gao, E., Zhou, B., Zhang, Z. & Xu, G., 2014. A successive three-point perturbation method for fast ray tracing in complex 2D and 3D geological models, *Tectonophysics,* **627,** 72–81.

Xu, T., Xu, G., Gao, E., Li, Y., Jiang, X. & Luo, K., 2006. Block modeling and segmentally iterative ray tracing in complex 3D media, *Geophysics,* **71,** T41–T51.

Xu, T., Zhang, Z., Gao, E., Xu, G. & Sun, L., 2010. Segmentally iterative ray tracing in complex 2D and 3D heterogeneous block models, *Bull. seism. Soc. Am.,* **100,** 841–850.

Xue, Q., Wang, Y. & Chang, X., 2016. Fast 3D elastic micro-seismic source location using new GPU features, *Phys. Earth planet. Inter.,* **261,** 24–35.

Zhang, H., Thurber, C. & Rowe, C., 2003. Automatic P-wave arrival detection and picking with multiscale wavelet analysis for single-component recordings, *Bull. seism. Soc. Am.,* **93,** 1904–1912.

Zhen, X., Li, Q., Zhang, Y., Bi, X. & Jin, S., 2016. Segmentation of crustal velocity structure beneath the Shandong-Jiangsu-Anhui segment of the Tanlu fault zone and adjacent areas and its geological interpretations, *Chin. J. Geophys.,* **59,** 691–702.

APPENDIX A: VECTOR RAY-TRACING FORMULAE

In Fig. 7, seismic waves strike an interface Σ separating an upper layer with velocity V_1 from a lower layer with velocity V_2. The geometry of the interface can be described by its elevation $z(x, y)$, and therefore the normal to the interface, $\hat{\mathbf{n}}$, is parallel to the vector $\mathbf{m} = \left(\frac{\partial z}{\partial x}, \frac{\partial z}{\partial y}, -1 \right)$. A seismic ray leaving point $\mathbf{P}_1$ (with coordinates (x_1, y_1, z_1)) in the upper layer penetrates through the interface at $\mathbf{P}_0$ (with coordinates (x, y, z)) and arrives at point $\mathbf{P}_2$ (with coordinates (x_2, y_2, z_2)) in the lower layer. This seismic ray can be also reflected at $\mathbf{P}_0$ back to the top layer at $\mathbf{P}_3$ (with coordinates (x_3, y_3, z_3)). In this section, we derive the relationship between the incident, reflected and transmitted ray vectors based on *Fermat's principle*. Although some of the conclusions are well known, the derivation itself is still non-trivial when the interface is not flat. For simplicity, we define the distance between $\mathbf{P}_1$ and $\mathbf{P}_0$, $\mathbf{P}_0$ and $\mathbf{P}_2$, $\mathbf{P}_0$ and $\mathbf{P}_3$, as well as the unit vectors for the incident, transmitted and

reflected ray direction as

$$R_1 = \|\mathbf{P}_0 - \mathbf{P}_1\| \quad R_2 = \|\mathbf{P}_2 - \mathbf{P}_0\| \quad \text{and} \quad R_3 = \|\mathbf{P}_3 - \mathbf{P}_0\|, \tag{A1}$$

$$\mathbf{r}_1 = \frac{\mathbf{P}_0 - \mathbf{P}_1}{R_1}, \quad \mathbf{r}_2 = \frac{\mathbf{P}_2 - \mathbf{P}_0}{R_2}, \quad \text{and} \quad \mathbf{r}_3 = \frac{\mathbf{P}_3 - \mathbf{P}_0}{R_3}, \tag{A2}$$

where $\| \cdot \|$ is the norm of a vector.

If the positions of $\mathbf{P}_1$ and $\mathbf{P}_2$ are fixed, then the traveltimes of seismic rays connecting $\mathbf{P}_1$ and $\mathbf{P}_2$ through $\mathbf{P}_0$ vary only as a function of $\mathbf{P}_0$ position on the interface, given by

$$T[x, y, z(x, y)] = \frac{R_1}{V_1} + \frac{R_2}{V_2}$$
$$= \frac{1}{V_1}\left[(x - x_1)^2 + (y - y_1)^2 + (z - z_1)^2\right]^{1/2} + \frac{1}{V_2}\left[(x_2 - x)^2 + (y_2 - y)^2 + (z_2 - z)^2\right]^{1/2}. \tag{A3}$$

Based on *Fermat's principle*, the partial derivatives of this traveltime vanish

$$\frac{\partial T}{\partial x} = \frac{\partial T}{\partial y} = 0. \tag{A4}$$

Let $\alpha = \frac{V_2}{V_1}, m_x = \frac{\partial z}{\partial x}, m_y = \frac{\partial z}{\partial y}, \|\mathbf{m}\| = m$, such that $m^2 = m_x^2 + m_y^2 + 1$, and $(r_{1x}, r_{1y}, r_{1z}), (r_{2x}, r_{2y}, r_{2z}), (r_{3x}, r_{3y}, r_{3z})$ be the three components of the unit vectors $\mathbf{r}_1, \mathbf{r}_2, \mathbf{r}_3$, respectively. Also note that

$$\frac{\partial R_1}{\partial x} = r_{1x} + r_{1z}m_x, \quad \frac{\partial R_1}{\partial y} = r_{1y} + r_{1z}m_y, \quad \frac{\partial R_2}{\partial x} = r_{2x} + r_{2z}m_x, \quad \frac{\partial R_2}{\partial y} = r_{2y} + r_{2z}m_y,$$

then eq. (A4) gives

$$r_{2x} + r_{2z}m_x = \alpha(r_{1x} + r_{1z}m_x), \quad r_{2y} + r_{2z}m_y = \alpha(r_{1y} + r_{1z}m_y). \tag{A5}$$

The three components of unit transmitted ray vector, $\mathbf{r}_2$ also satisfies

$$r_{2x}^2 + r_{2y}^2 + r_{2z}^2 = 1. \tag{A6}$$

From eqs (A5) and (A6), we can solve for the three components of transmitted ray vector $\mathbf{r}_2$ as

$$r_{2z} = \frac{\alpha\left[r_{1x}m_x + r_{1y}m_y + r_{1z}(m_x^2 + m_y^2)\right] \pm B^{1/2}}{m^2}, \tag{A7}$$

$$r_{2x} = \alpha(r_{1x} + r_{1z}m_x) - r_{2z}m_x, \tag{A8}$$

$$r_{2y} = \alpha(r_{1y} + r_{1z}m_y) - r_{2z}m_y, \tag{A9}$$

where the variable B is given by

$$B = m^2 - \alpha^2\left[(r_{1y}m_x - r_{1x}m_y)^2 + (r_{1x} + r_{1z}m_x)^2 + (r_{1y} + r_{1z}m_y)^2\right]. \tag{A10}$$

Clearly, transmitted waves only exist when $B \geq 0$. If we define the angle between $\mathbf{r}_1$ vector and $\mathbf{m}$ vector as θ_1 (i.e. incident angle), and the angle between $\mathbf{r}_2$ and $\mathbf{m}$ as θ_2 (i.e. transmission angle), where $\theta_1, \theta_2 \in [0, \pi)$, then

$$\mathbf{r}_1 \cdot \mathbf{m} = r_{1x}m_x + r_{1y}m_y - r_{1z} = m\cos\theta_1, \quad \mathbf{r}_2 \cdot \mathbf{m} = r_{2x}m_x + r_{2y}m_y - r_{2z} = m\cos\theta_2 \tag{A11}$$

and

$$(r_{1y}m_x - r_{1x}m_y)^2 + (r_{1x} + r_{1z}m_x)^2 + (r_{1y} + r_{1z}m_y)^2 = \|\mathbf{r} \times \mathbf{m}\|^2 = m^2\sin^2\theta. \tag{A12}$$

Therefore eq. (A10) becomes

$$B = m^2(1 - \alpha^2\sin^2\theta), \tag{A13}$$

which is non-negative only under the well-known condition that

$$\sin\theta_1 \leq \frac{V_1}{V_2}. \tag{A14}$$

When the velocity speed in the upper medium is faster than or equal to that of the lower medium, $V_1 \geq V_2$, the above expression always holds. However, when $V_1 < V_2$, the seismic ray transmits from a low-velocity medium to a fast-velocity medium, the incident angle has to be less than or equal to $\sin^{-1}(V_1/V_2)$ for the transmitted waves to exist, otherwise only evanescent waves (i.e. head waves) exist in the faster-velocity medium.

To see how the $\pm$ sign should be picked in eq. (A7), using eqs (A7)–(A9), we have

$$m \cos \theta_2 = \mathbf{r}_2 \cdot \mathbf{m} = r_{2x} m_x + r_{2y} m_y - r_z$$
$$= \alpha[(r_{1x} + r_{1z} m_x) m_x + (r_{1y} + r_{1z} m_y) m_y] - r_{2z}(m_x^2 + m_y^2 + 1)$$
$$= \alpha[r_{1x} m_x + r_{1y} m_y + r_{1z}(m_x^2 + m_y^2)] - r_{2z} m^2, \tag{A15}$$

and hence

$$r_{2z} = \frac{\alpha[r_{1x} m_x + r_{1y} m_y + r_{1z}(m_x^2 + m_y^2)] - m \cos \theta_2}{m^2}. \tag{A16}$$

Comparing eq. (A16) with eq. (A7), we can pick the correct sign for the r_{2z} expression as

$$r_{2z} = \frac{\alpha[r_{1x} m_x + r_{1y} m_y + r_{1z}(m_x^2 + m_y^2)] - \mathrm{sgn}(\cos \theta_2) B^{1/2}}{m^2} \tag{A17}$$

which also requires that

$$B^{1/2} = m(1 - \alpha^2 \sin \theta_1)^{1/2} = m \| \cos \theta_2 \| \tag{A18}$$

or

$$\frac{\sin \theta_1}{V_1} = \frac{\sin \theta_2}{V_2}, \tag{A19}$$

which is the *Snell's law*, a natural corollary following the *Format's Principle*. Since the incident and transmitted ray vectors, $\mathbf{r}_1$ and $\mathbf{r}_2$ are in the same general direction, we have

$$\mathrm{sgn}(\cos \theta_2) = \mathrm{sgn}(\cos \theta_1) = \mathrm{sgn}(\mathbf{r}_1 \cdot \mathbf{m}) \tag{A20}$$

and can help rewrite r_{2z} to a function of only the incident ray vector and interface normal,

$$r_{2z} = \frac{\alpha[r_{1x} m_x + r_{1y} m_y + r_{1z}(m_x^2 + m_y^2)] - \mathrm{sgn}(r_{1x} m_x + r_{1y} m_y - r_{1z}) B^{1/2}}{m^2}. \tag{A21}$$

Similarly, we minimize the traveltime for the ray path between $\mathbf{P}_1$ and $\mathbf{P}_0$, and $\mathbf{P}_0$ and $\mathbf{P}_3$,

$$T[x, y, z(x, y)] = \frac{R_1}{V_1} + \frac{R_3}{V_2} \tag{A22}$$

to obtain the reflection vector $\mathbf{r}_3$ as

$$r_{3z} = \frac{[r_{1x} m_x + r_{1y} m_y + r_{1z}(m_x^2 + m_y^2)] \pm C^{1/2}}{m^2}, \tag{A23}$$

$$r_{3x} = r_{1x} + r_{1z} m_x - r_{2z} m_x, \tag{A24}$$

$$r_{3y} = r_{1y} + r_{1z} m_y - r_{2z} m_y, \tag{A25}$$

where

$$C = m^2 - [(r_{1y} m_x - r_{1x} m_y)^2 + (r_{1x} + r_{1z} m_x)^2 + (r_{1y} + r_{1z} m_y)^2] = m^2 \cos \theta_1^2. \tag{A26}$$

Now we define the angle between the reflection ray vector $\mathbf{r}_3$ and m to be θ_3', which is supplementary to the reflection angle θ_3 (Fig. 7), and using eqs (A23)–(A25), we have

$$m \cos \theta_3' = \mathbf{r}_3 \cdot \mathbf{m} = r_{3x} m_x + r_{3y} m_y - r_{3z} = r_{1x} m_x + r_{1y} m_y + (m_x^2 + m_y^2) r_{1z} - r_{3z} m^2 \tag{A27}$$

and

$$r_{3z} = \frac{r_{1x} m_x + r_{1y} m_y + (m_x^2 + m_y^2) r_{1z} - m \cos \theta_3'}{m^2} \tag{A28}$$

which when compared to eq. (A23) helps us pick the $\pm$ sign in the r_{3z} expression as

$$r_{3z} = \frac{[r_{1x} m_x + r_{1y} m_y + r_{1z}(m_x^2 + m_y^2)] - \mathrm{sgn}(\cos \theta_3') C^{1/2}}{m^2} \tag{A29}$$

and requires

$$C = m^2 \cos \theta_1^2 = m^2 \cos^2 \theta_3'. \tag{A30}$$

Note that because the reflected ray vector returns to the upper layer, $\mathrm{sgn}(\cos \theta_1) = -\mathrm{sgn}(\cos \theta_3') = \mathrm{sgn}(\cos \theta_3)$. Therefore eq. (A30) can be simplified to $\cos \theta_1 = \cos \theta_3$, or simply $\theta_1 = \theta_3$, that is, the well-known result that *P* reflection angle is the same as the *P* incident angle.

Eq. (A29) can be further reduced to

$$
r_{3z} = \frac{\left[r_{1x}m_x + r_{1y}m_y + r_{1z}(m_x^2 + m_y^2) \right] + m \cos \theta_1}{m^2}
$$
$$
= \frac{2(r_{1x}m_x + r_{1y}m_y) + r_{1z}(m_x^2 + m_y^2 - 1)}{m^2}. \tag{A31}
$$

Hence, given the incident ray vector $\mathbf{r}_1$, the reflected and transmitted ray vectors, $\mathbf{r}_2$ and $\mathbf{r}_3$, can be found accordingly if the normal of the interface at the incident point $\mathbf{P}_0$ is known.

In practice, as the *Snell's law* (eq. A19) is true for any two layers, if the incident wave arriving angle θ_1 is already determined for the surface layer (with P velocity V_1), then the back-traced ray can never penetrate deeper than the kth layer with P-velocity $V_k \geq V_1/\sin\theta_1$. And if the ray terminal of this particular ray deviates significantly from other rays, or the ray has arrived back to the surface before other ray terminals show signs of convergence, this ray must have been critically reflected, and the background model needs to be adjusted to avoid these situations.